Publishing Excellence
Inspiring Progress

ISSN: 3143-0732 https://aristonpubs.com/journal/science-of-alloys-and-glasses https://doi.org/10.69626/sag.2025.0038

RESEARCH ARTICLE

Investigating Radiation Shielding Efficiency and *In–Vitro* Biological Performance of Modified Tellurite Glasses

Lama H. Alhayaza [1], Rana S. Alayyash [1,*], Hajar S. Alqahtani [1], Haifa H. Alqahtani [1], Roaa A. Asiri [1], Sarah M. Alshehri [1], Mohammad Abohassan [2, 3]

ABSTRACT: This study comprehensively examines the radiation shielding capabilities and in vitro biological properties of tellurite-based glasses modified with various heavy metal oxides. A series of glasses with the nominal composition (85-x)TeO_2–5Nb_2O_5–xZnO, incorporating distinct modifiers (5Ag_2O, 7PbO, 18PbO, and 7Na_2O in mol%), were investigated. The photon attenuation characteristics were evaluated computationally using MIKE simulation software across a broad energy spectrum (0.015–15 MeV). Key shielding parameters, including mass and linear attenuation coefficients (MAC, LAC), half-value layer (HVL), mean free path (MFP), and effective atomic number (Zeff), were determined. Results indicate a direct correlation between shielding performance and material density, with the 18 mol% PbO-doped glass exhibiting the most promising attenuation properties. This sample achieved the highest MAC and Zeff values, along with the lowest HVL and MFP, confirming superior gamma-ray shielding efficacy. Furthermore, the in vitro biological activity of the glass compositions was assessed. Antibacterial susceptibility tests revealed significant activity against Gram-positive bacteria, including *Staphylococcus aureus* and *Streptococcus pyogenes*, while effects on Gram-negative strains were minimal. Additionally, blood coagulation assays (PT and APTT) demonstrated that certain compositions could modulate clotting times, suggesting potential hemostatic applications. This dual functionality positions these modified tellurite glasses as promising candidates for advanced materials in both radiation protection and biomedical fields.

Keywords: Tellurite glass, Radiation shielding, Gamma-ray attenuation, Antibacterial activity, Hemostatic properties, Biocompatibility.

Received: 19 October 2024; Revised: 25 November 2024; Accepted: 02 January 2025; Published Online: 04 February 2025

1. INTRODUCTION

The imperative for effective radiation shielding has grown substantially over recent decades, paralleling the expanding use of ionizing radiation across medical diagnostics, cancer therapy, nuclear energy, and industrial non-destructive testing. While these technologies offer immense societal benefits, they inherently pose significant health risks to occupationally exposed personnel and the public. Exposure to ionizing radiation can induce a spectrum of detrimental biological effects, ranging from deterministic tissue damage at high doses to an increased probability of stochastic effects, such as carcinogenesis and genetic mutations, even at lower exposure levels [1]. Consequently, implementing robust safety protocols is not merely a regulatory formality but a fundamental ethical obligation. The cornerstone of radiological protection is the ALARA principle, which is operationalized through a triad of measures: minimizing exposure time, maximizing distance from the source, and

[1] Department of Radiological Sciences, College of Applied Medical Sciences, King Khalid University, AlQuraa, Abha, P. O. Box 906, Saudi Arabia
[2] Department of Clinical Laboratory Sciences, College of Applied Medical Sciences, King Khalid University, Abha, Saudi Arabia.
[3] Health and Medical Research Centre, King Khalid University, Abha 61421, Saudi Arabia

* Author to whom correspondence should be addressed: ranasaalayash@gmail.com (Rana S. Alayyash)

© Ariston Publications 2025. All rights reserved.

employing effective shielding barriers. Among these, physical shielding is often the most critical and reliable component for attenuating radiation to safe levels [2-5].

The efficacy of a material in attenuating X-rays and gamma rays is fundamentally governed by its density (ρ) and effective atomic number (Z_{eff}). Photon interaction probabilities, via the photoelectric effect, Compton scattering, and pair production, scale favorably with these parameters. For decades, lead (Pb) and lead-based composites have been the industry standard for shielding due to their high density (11.34 g/cm³), high atomic number (82), relatively low cost, and ease of fabrication [6-13]. However, the severe neurotoxicity and environmental persistence of lead have prompted a global reassessment of its use. Its disposal presents significant hazards, and its opacity and weight limit design flexibility in applications requiring visibility or structural lightness. This has catalyzed an intensive search for non-toxic, high-performance alternative materials that can match or exceed lead's shielding capacity.

In this context, amorphous glassy materials have emerged as exceptionally promising candidates. Unlike crystalline shields, glasses offer a unique combination of properties highly desirable for practical applications: excellent optical transparency in tailored compositions, superior resistance to environmental corrosion, inherent homogeneity, ease of fabrication into complex shapes (sheets, fibers, blocks), and tunable mechanical properties [14, 15]. The shielding performance of a glass is not intrinsic but is a direct function of its chemical composition. By incorporating high concentrations of heavy metal oxides (HMOs), such as bismuth oxide (Bi_2O_3), barium oxide (BaO), tungsten oxide (WO_3), or lead oxide (PbO), into the glass network, its density and effective atomic number can be dramatically increased, thereby enhancing its photon-stopping power [16-18]. Among various glass families, heavy-metal oxide glasses based on tellurium dioxide (TeO_2) have attracted particular interest. Tellurite glasses possess a distinctive set of advantages, including a relatively low melting temperature, high refractive index, broad infrared transmission window, good chemical durability, and high solubility for rare-earth and transition metal ions [19-21]. These attributes make them suitable not only for shielding but also for photonic and sensing applications. The radiation attenuation performance of a tellurite glass system is quantified through key parameters such as the mass attenuation coefficient (μ/ρ), linear attenuation coefficient (μ), half-value layer (HVL), mean free path (MFP), and effective atomic number (Z_{eff}), all of which are strongly influenced by the type and concentration of modifying oxides.

The strategic incorporation of specific network modifiers can tailor both the structural and functional properties of tellurite glasses. For instance, zinc oxide (ZnO) acts as a network modifier that can enhance the chemical durability of the glass, lower its crystallization tendency, and influence its optical nonlinearity [22]. Niobium pentoxide (Nb_2O_5) is particularly interesting due to its dual role as both a network modifier and a conditional network former, which can improve the thermal stability and mechanical strength of the glass matrix [23, 24]. This study focuses on synthesizing and characterizing a series of tellurite glasses with the composition (85-x)TeO_2 – 5Nb_2O_5 – xZnO, further modified with distinct heavy metal oxides: 5Ag_2O, 7PbO, 18PbO, and 7Na_2O (in mol%). A comprehensive analysis of their gamma-ray shielding capacity across a broad energy spectrum (0.015–15 MeV) forms the core of this investigation.

The novelty of this research lies in its integrative approach, which moves beyond a singular focus on radiation physics to encompass preliminary assessments of in vitro biological compatibility, thereby probing the potential for multifunctional application. While the shielding efficiency of tellurite glasses is well-documented, their combined interaction with biological systems, particularly concerning antimicrobial activity and blood coagulation pathways, remains a relatively underexplored frontier with significant implications for biomedical use. Biomaterials intended for use in medical environments, such as radiotherapy suites or diagnostic imaging rooms, must not only provide protection but also interface safely with biological tissues. A critical aspect of this biocompatibility is the material's interaction with blood, the primary fluid encountering any implant or device. Upon contact, blood plasma proteins rapidly adsorb onto a material's surface, triggering a cascade of responses including platelet adhesion, activation, and the coagulation cascade [25-29]. Nanomaterials and certain ions, such as silver (Ag^+), are known to interact with coagulation factors and cellular components, which can be either detrimental, potentially increasing thrombotic risk [30], or beneficial, offering opportunities for developing pro-coagulant agents for hemorrhage control or anticoagulant therapies [31]. Furthermore, the intrinsic antimicrobial properties of ions like Ag^+ are well-established, suggesting that glasses incorporating such modifiers could also mitigate infection risks [32]. Therefore, this work adopts a dual-purpose design strategy. Alongside a detailed computational and theoretical evaluation of radiation shielding parameters using MIKE software, we conduct an initial in vitro biological screening. This includes assessing the antibacterial efficacy of the glass compositions against a panel of clinically relevant Gram-positive and Gram-negative pathogens and evaluating their influence on the blood coagulation cascade via standardized assays for Prothrombin Time (PT) and Activated Partial Thromboplastin Time (APTT). This combined physicochemical and biological profiling aims to identify tellurite glass compositions that offer not only superior radiation attenuation but also potentially beneficial interactions with biological systems, paving the way for their development as advanced multifunctional materials for medical and protective applications.

2. EXPERIMENTAL DETAILS

2.1. Computational Shielding Analysis with MIKE Software

The radiation shielding characteristics of the designed

© Ariston Publications 2025. All rights reserved.

tellurite glass compositions were determined computationally using the MIKE (Computerized Software for Radiation Shielding Characteristics) simulation platform. MIKE is a specialized software tool designed to calculate fundamental parameters that define a material's interaction with ionizing radiation. Its algorithms are based on established photon cross-section databases, such as those from NIST (National Institute of Standards and Technology), ensuring reliable and physics-based predictions. For this study, the primary function of the software was to calculate key gamma-ray attenuation parameters across a defined energy spectrum. By inputting the precise elemental composition and weight fractions of each glass sample, derived from the nominal molar formulas (85-x)TeO_2, 5Nb_2O_5, xZnO, plus the respective modifiers (5Ag_2O, 7PbO, 18PbO, 7Na_2O), the software computes essential metrics. These include the mass attenuation coefficient (μ/ρ), the linear attenuation coefficient (μ), the half-value layer (HVL), and the tenth-value layer (TVL). Furthermore, MIKE can be utilized to derive related physical and optical properties of the glass compositions, such as the average molar weight, molar volume, and molar electronic polarizability, providing a more comprehensive material profile.

2.2. Theoretical Framework for Radiation Attenuation

The mass attenuation coefficient (μ/ρ) is defined by Eq. 1 [1-7] as a composition-dependent quantity. The following formula is used to compute the glasses under consideration of the linear attenuation coefficients (μ) of the:

$$\mu/\rho = \sum i\, w_i(\frac{\mu}{\rho})_i \quad (1)$$

$$\mu = \frac{ln\frac{I}{I_0}}{d} \quad (2)$$

The tenth-value layer (TVL) and half-value layer (HVL) define the thickness of the acting target at which the attenuated intensities are 90% and 50% of the narrow photon beam intensity, respectively. In contrast, the mean free path (MFP) is the average distance a photon travels in the barrier before interacting, and is denoted μ. It is obtained by multiplying the corresponding μ/ρ value by density. The required thickness of the shielding material is inversely proportional to the TVL and HVL. As a result, it can be calculated as equation (1), where w_i and (μ/ρ) i denote the weight fraction and mass attenuation coefficient values (cm^2/g) of the i^{th} constituent in the glass, respectively. where (μ,d, $I_0$and I) reveal the linear attenuation coefficient and the thickness of the glass (cm^{-1}), is the amount of concrete, I_0 and I Constitute the recorded counts in the detector with and without glass, accordingly.

$$HVL = \frac{0.693}{\mu} \quad (3)$$

$$TVL = \frac{Ln10}{\mu} \quad (4)$$

$$MFP = \frac{1}{\mu} \quad (5)$$

σ_a can be obtained from Eq. (6), where fi is the fractional abundance and Z_i is the atomic number of each component in the target. Z_i can be determined by dividing the molecular cross-section (σ_m) by the total number of formula units.

$$\sigma_a = \sigma_m \ \frac{1}{\sum i\ ni}\frac{(\mu/\rho)target}{N_A \sum i\frac{wi}{Ai}} \quad (6)$$

$$Z_{eff} = \frac{\sigma_a}{\sigma_e} \quad (7)$$

$$N_{eff} = N\frac{Z_{eff}}{\sum i\ fiAi} \quad (8)$$

2.3. Antibacterial Susceptibility Assay via Well Diffusion Method

The in vitro antibacterial potential of the synthesized glass compounds was evaluated against a panel of clinically relevant bacterial strains using the standardized agar well diffusion method. The microbial panel included both Gram-negative and Gram-positive pathogens: *Pseudomonas aeruginosa*, *Enterococcus faecalis, Streptococcus pyogenes*, *Escherichia coli*, *Staphylococcus aureus*, *Staphylococcus Salmonella* spp., *Klebsiellapneumoniae*, and *saprophyticus*. Each bacterial strain was first cultured in nutrient broth and incubated until reaching the mid-logarithmic growth phase, corresponding to an optical density at 600 nm (OD600) between 0.4 and 0.6. The bacterial suspensions were then standardized by dilution in fresh broth to a theoretical OD600 of 0.01, ensuring a consistent and confluent lawn of growth.

Nutrient agar plates were prepared and sterilized according to standard microbiological protocols. Using a sterile swab, the standardized bacterial suspension was uniformly spread across the entire surface of each agar plate to create a bacterial lawn. Subsequently, wells of 6.0 mm diameter were aseptically punched into the solidified agar using a sterile syringe cap or cork borer. A measured volume of 20 μL of each test compound, prepared as a 2 mg/mL aqueous suspension or extract, was carefully pipetted into the designated wells. The plates were then left at room temperature for approximately 15 minutes to allow for compound diffusion into the agar before being inverted and transferred to a 37°C incubator for 24 hours of aerobic incubation [33, 34]. Following incubation, the diameter of any clear, circular zone of inhibition (ZOI) surrounding the well, indicating inhibition of bacterial growth, was measured in millimeters using a precision caliper. The antibacterial activity was quantified by subtracting the well diameter (6 mm) from the total inhibition zone diameter to obtain the zone of bacterial growth inhibition attributable solely to the compound.

2.4. Bacterial Growth Kinetic Assay

© Ariston Publications 2025. All rights reserved.

To complement the endpoint analysis of the well diffusion test and to assess the dynamic effect of the glass compounds on bacterial proliferation, a growth kinetic assay was performed. This time-kill study monitors changes in the optical density of a bacterial culture over time, providing information on whether a compound is bacteriostatic (inhibits growth) or bactericidal (kills cells). For this assay, a 96-well microtiter plate format was employed. Each well received 180 µL of a fresh bacterial culture, standardized to an initial OD600 of 0.01. To this, 20 µL of the respective glass compound suspension (2 mg/mL) was added, resulting in a final test compound concentration. Control wells containing 180 µL of bacterial culture and 20 µL of sterile distilled water or solvent were included to represent normal, unimpeded bacterial growth.

The sealed microtiter plate was then placed in a FLUOstar Omega microplate reader (BMG Labtech, Germany), which was pre-programmed for kinetic cycle measurements. The plate was incubated at 37°C with continuous shaking for a total duration of 16 hours. The optical density at 600 nm (OD600) of each well was automatically measured at regular intervals of 2 hours. This wavelength is optimal for tracking bacterial cell density, as it minimizes interference from the test compounds. The entire experiment was performed in triplicate to ensure statistical reliability. The mean absorbance values from the triplicate readings were plotted against time to generate growth curves for each bacterial strain in the presence and absence of the test compounds. A significant suppression of the growth curve slope or a lower final OD600 in treated samples compared to the control directly indicates antimicrobial activity.

2.5. In Vitro Blood Coagulation Assays

The potential influence of the glass components on the blood coagulation cascade was investigated using two standard clinical hematological tests: the Prothrombin Time (PT) and the Activated Partial Thromboplastin Time (APTT). These assays evaluate the extrinsic and intrinsic pathways of coagulation, respectively. Human venous blood was collected from healthy, consenting donors using vacuum tubes containing 3.2% buffered sodium citrate as an anticoagulant, in a standard ratio of 1 part anticoagulant to 9 parts blood. To obtain platelet-poor plasma (PPP), essential for these tests, the citrated blood was centrifuged at 1500 × g for 10 minutes at room temperature. The resulting supernatant plasma was carefully aspirated and used immediately.

For the Prothrombin Time (PT) assay, which assesses the extrinsic and common pathways, 5 mg of each glass compound (in powdered form) was placed into a pre-warmed test tube. To this, 50 µL of PPP was added, and the mixture was incubated for precisely 2 minutes in a 37°C water bath to allow for any potential plasma-factor interaction. Coagulation was then initiated by the rapid addition of 100 µL of pre-warmed commercial PT reagent (containing tissue factor and calcium). A stopwatch was started simultaneously, and the tube was gently tilted at regular intervals. The time in seconds from reagent addition to the first visible formation of a fibrin clot was recorded as the PT. A negative control, consisting of PPP and reagent without any test compound, was always run in parallel for baseline comparison, following CLSI guideline H3-A5.

The Activated Partial Thromboplastin Time (APTT) assay, probing the intrinsic and common pathways, followed a similar but distinct protocol. A test tube containing 5 mg of the glass compound received 100 µL of PPP and 100 µL of APTT reagent (containing a phospholipid emulsion and a contact activator like kaolin or silica). This mixture was incubated at 37°C for exactly 2 minutes to allow for contact activation. Subsequently, 50 µL of pre-warmed 0.2 M calcium chloride ($CaCl_2$) solution was added to re-calcify the plasma and trigger the coagulation cascade. The time from the addition of calcium chloride to the formation of a fibrin clot was recorded as the APTT. Again, a negative control without any test compound was included. Significant shortening of PT or APTT compared to the control would suggest a pro-coagulant effect, while prolongation would indicate anticoagulant activity.

3. RESULTS AND DISCUSSION

3.1. Radiation Shielding Parameters

The gamma-ray shielding characteristics of the four synthesized tellurite glass compositions, designated as Sample A ($5Ag_2O$), Sample B ($7Na_2O$), Sample C (18PbO), and Sample D (7PbO), were systematically evaluated over a broad energy spectrum from 0.015 to 15 MeV using the MIKE simulation software. The primary parameter for assessing intrinsic photon interaction probability is the mass attenuation coefficient (MAC, μ/ρ). Figure 1 illustrates the variation of MAC with incident photon energy for all four samples. A pronounced and consistent trend is observed: MAC values are exceptionally high at the lowest energy (0.015 MeV) and undergo a sharp, exponential decrease as energy increases up to approximately 0.1 MeV. This steep decline is characteristic of the photoelectric absorption process, the dominant interaction mechanism at low energies, where the cross-section is proportional to approximately Z^4/E^3 (Z is the atomic number, E is the photon energy). Beyond 0.1 MeV, the rate of decrease diminishes significantly, and the MAC values enter a region of gradual decline throughout the intermediate energy range (0.1 – 5 MeV). This plateau-like behavior signifies the dominance of Compton scattering, a process where the cross-section per electron is largely independent of atomic number and decreases only slowly with increasing energy. Among the samples, Sample C (18PbO) consistently exhibits the highest MAC values across the entire energy range. This superior performance is directly attributable to its high lead content; lead (Pb, Z=82) has a significantly higher atomic number and photoelectric cross-section compared to sodium (Na, Z=11)

© Ariston Publications 2025. All rights reserved.

or silver (Ag, Z=47), leading to more effective photon attenuation per unit mass.

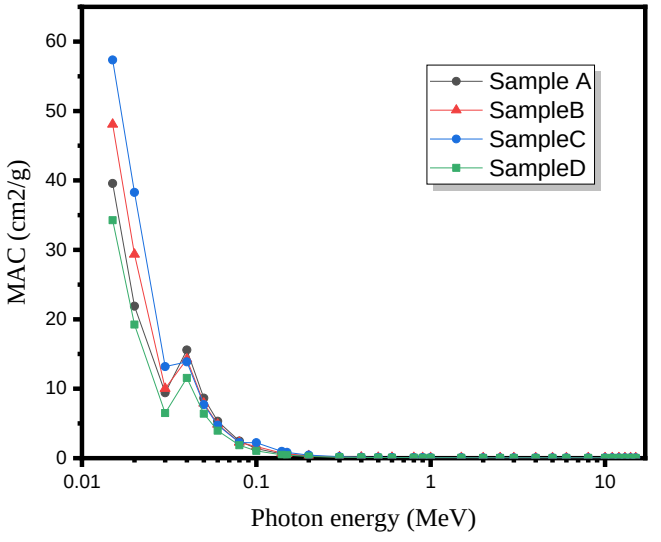


Fig. 1. Mass attenuation coefficients (MAC) of the prepared tellurite glasses (Sample A: $5Ag_2O$, Sample B: $7Na_2O$, Sample C: 18PbO, Sample D: 7PbO) as a function of photon energy in the range of 0.015 – 15 MeV.

While MAC describes the intrinsic property, the linear attenuation coefficient (LAC, μ) is a more practical measure as it incorporates the material's density ($\mu = (\mu/\rho) \times \rho$). Figure 2 presents the LAC for the glass samples. The energy-dependent trend mirrors that of the MAC, again showing the sharp drop in the photoelectric region and the gradual decline in the Compton region. The ranking of the samples, however, is dictated by both their MAC and their density. Sample C, with the highest lead content and consequently the highest density, demonstrates the greatest LAC at any given energy. The maximum LAC values at 0.015 MeV were calculated as 212.641, 272.270, 348.304, and 185.476 cm^{-1} for Samples A, B, C, and D, respectively. This order (C > B > A > D) underscores the profound impact of PbO concentration. Sample B ($7Na_2O$) shows a higher LAC than Sample A ($5Ag_2O$) despite sodium's lower Z, which may be attributed to a combination of its higher modifier concentration affecting density and the specific composite cross-section of the overall matrix. The high LAC of Sample C indicates a greater probability of photon interaction per centimeter of material, making it the most effective shield in terms of required thickness.

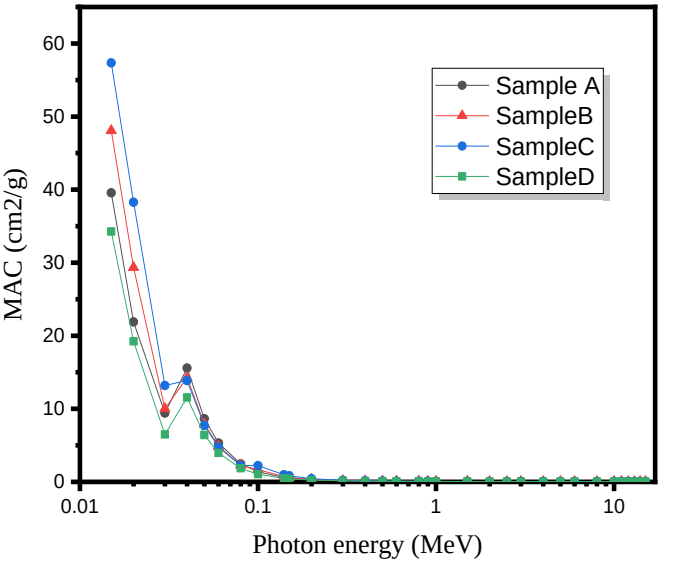


Fig. 2. Linear attenuation coefficients (LAC) of the prepared tellurite glasses as a function of photon energy (0.015 – 15 MeV).

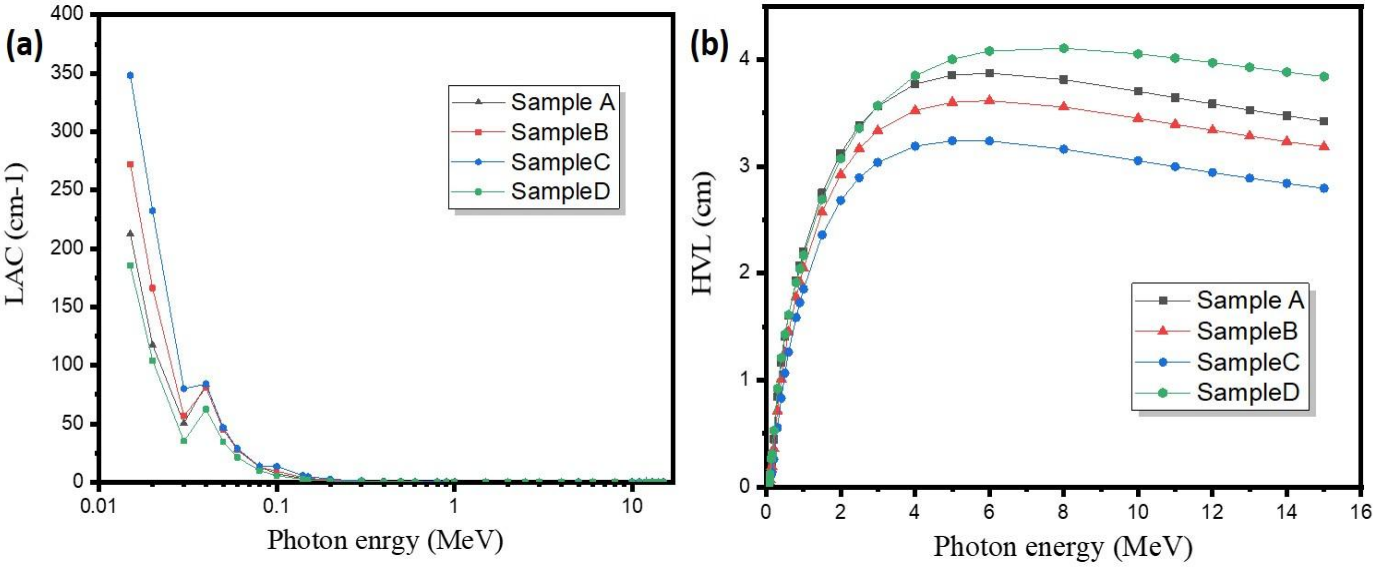


Fig. 3. (a) Half-value layer (HVL) and (b) Tenth-value layer (TVL) for the prepared glass samples as a function of photon energy (0.015 – 15 MeV).

© Ariston Publications 2025. All rights reserved.

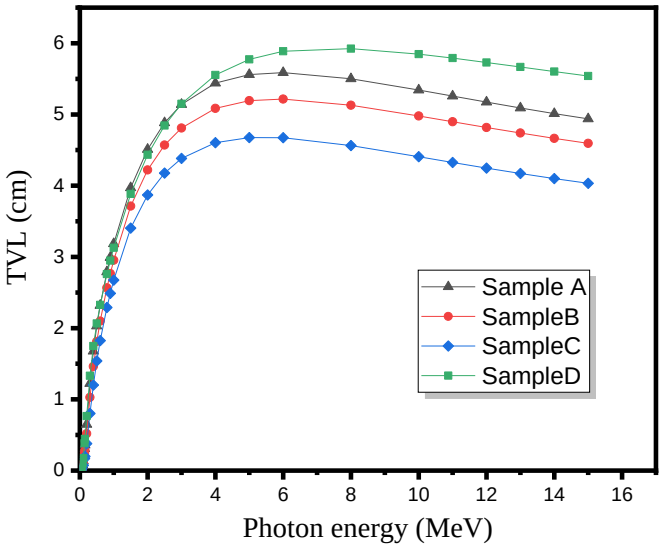


Fig. 4. Mean free path (MFP) for the prepared glass samples as a function of photon energy (0.015 – 15 MeV).

From the LAC, critical engineering parameters for shield design were derived: the half-value layer (HVL), the tenth-value layer (TVL), and the mean free path (MFP). The HVL (Figure 3(a) is the thickness required to reduce radiation intensity by half, calculated as HVL = 0.693/μ. The TVL (Figure 3b) is the thickness to reduce intensity to one-tenth, given by TVL = 2.303/μ. The MFP (Figure 4) is the average distance between photon interactions, defined as MFP = 1/μ. All three parameters share a fundamental inverse relationship with the LAC. Consequently, their plots show the opposite trend to Figures 1 and 2: values are very low at minimal energies and increase with photon energy.

For an ideal shielding material, low HVL, TVL, and MFP values are desired, as they indicate less material is needed for adequate attenuation. Sample C unambiguously possesses the lowest values for all three parameters across the energy spectrum. For instance, in the low-energy region where shielding is often most critical for containment, the HVL for Sample C is significantly smaller than for the other samples. This confirms that the 18 mol% PbO glass would require the thinnest barrier to achieve the same level of radiation protection. The steady rise in HVL, TVL, and MFP with energy reflects the decreasing interaction probability, necessitating thicker shields for higher-energy photons.

Further insight into the photon interaction mechanics is provided by the effective atomic number (Z_{eff}) and effective electron density (N_{eff}). Z_{eff} (Figure 5(a)) represents a weighted average atomic number for the composite material, indicative of its overall photon interaction cross-section. Its energy dependence is complex and revealing. At very low energies (0.015 MeV), Z_{eff} is at its maximum for all samples, heavily dominated by the photoelectric effect's strong Z^4 dependence. It then drops sharply to a broad minimum in the Compton scattering region (0.1 – 5 MeV), where interaction is less dependent on Z. Sample C exhibits the highest Z_{eff} values throughout, peaking at over 60 at 0.015 MeV, a direct consequence of its high lead fraction. Sample D (7PbO) follows, then Sample B and Sample A. This order correlates perfectly with the observed MAC and LAC rankings. Neff (Figure 5(b)), the number of electrons per unit mass, shows an almost identical energy-dependent profile to Z_{eff}, as it is directly proportional to it ($N_{eff} \propto Z_{eff}$ / Average Atomic Weight). The high N_{eff} of Sample C further explains its superior shielding; a greater electron density increases the probability of both photoelectric and Compton interactions. The steady decline in both $Z_{eff\ and}$ Neff through the Compton region and their very slight rise at high energies (due to the onset of pair production, which has a Z^2 dependence) are consistent with established theoretical behavior reported in the literature [35, 36].

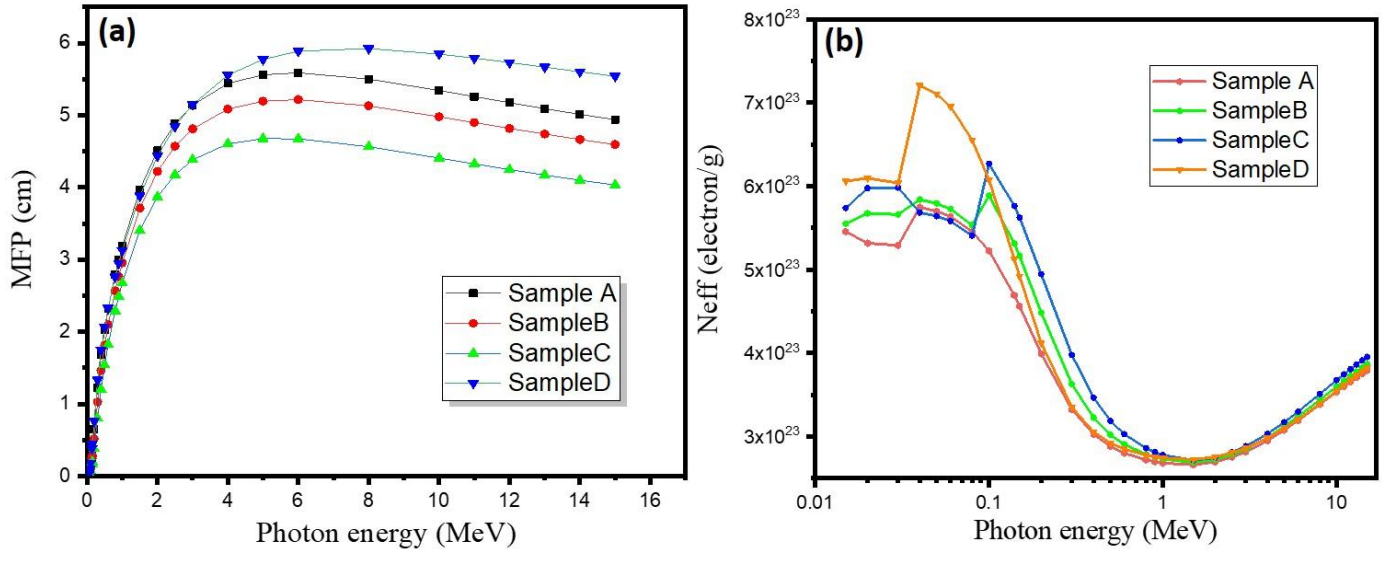


Fig. 5. (a) Effective atomic number (Z_{eff}) and (b) Effective electron density (N_{eff}) for the prepared tellurite glasses as a function of photon energy (0.015 – 15 MeV).

© Ariston Publications 2025. All rights reserved.

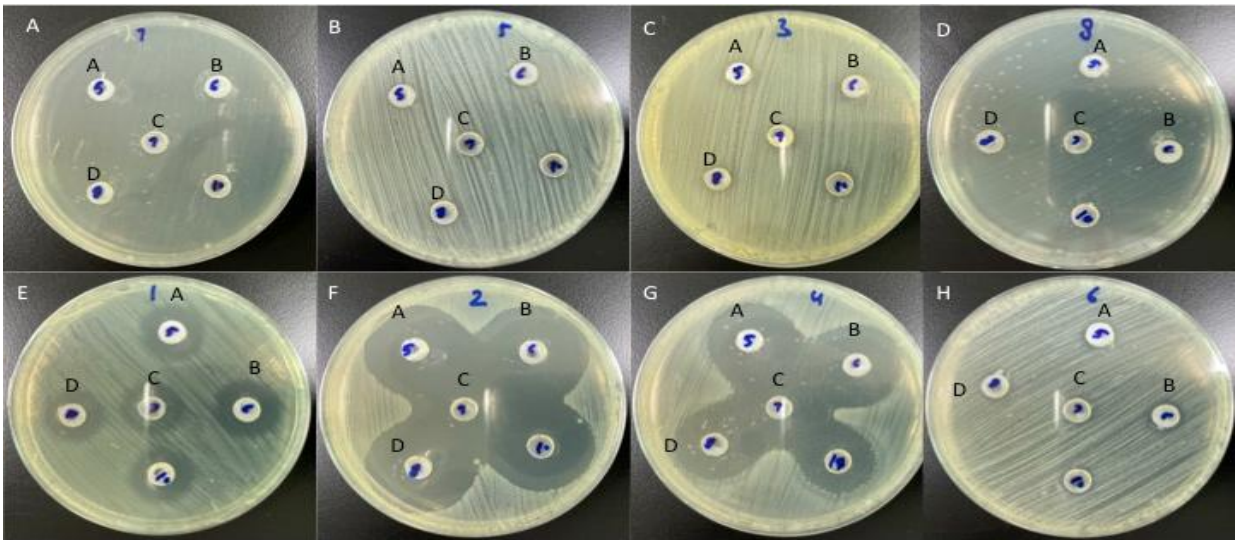


Fig. 6. Representative images of antibacterial activity assays (A-H) showing zones of inhibition produced by the synthesized compounds (A: Sample A, B: Sample B, C: Sample C, D: Sample D) against various bacterial strains.

3.2. Antibacterial Activity of the Synthesized Glasses

The in vitro antibacterial potential of the glass compounds was assessed against a panel of eight pathogenic bacteria using the agar well diffusion assay. The results, depicted in Figures 6 and 7, reveal a distinct and selective antibacterial profile. All four synthesized compounds (Samples A-D) demonstrated measurable antibacterial activity exclusively against Gram-positive bacteria. The Gram-positive strains tested, *Staphylococcus aureus*, *Staphylococcus saprophyticus*, *Streptococcus pyogenes*, and *Enterococcus faecalis,* showed clear zones of inhibition (ZOI) around the wells containing the glass suspensions. In contrast, no zone of inhibition was observed for any of the compounds against the Gram-negative strains: *Pseudomonas aeruginosa*, *Escherichia coli*, *Klebsiella pneumoniae*, and *Salmonella* spp.

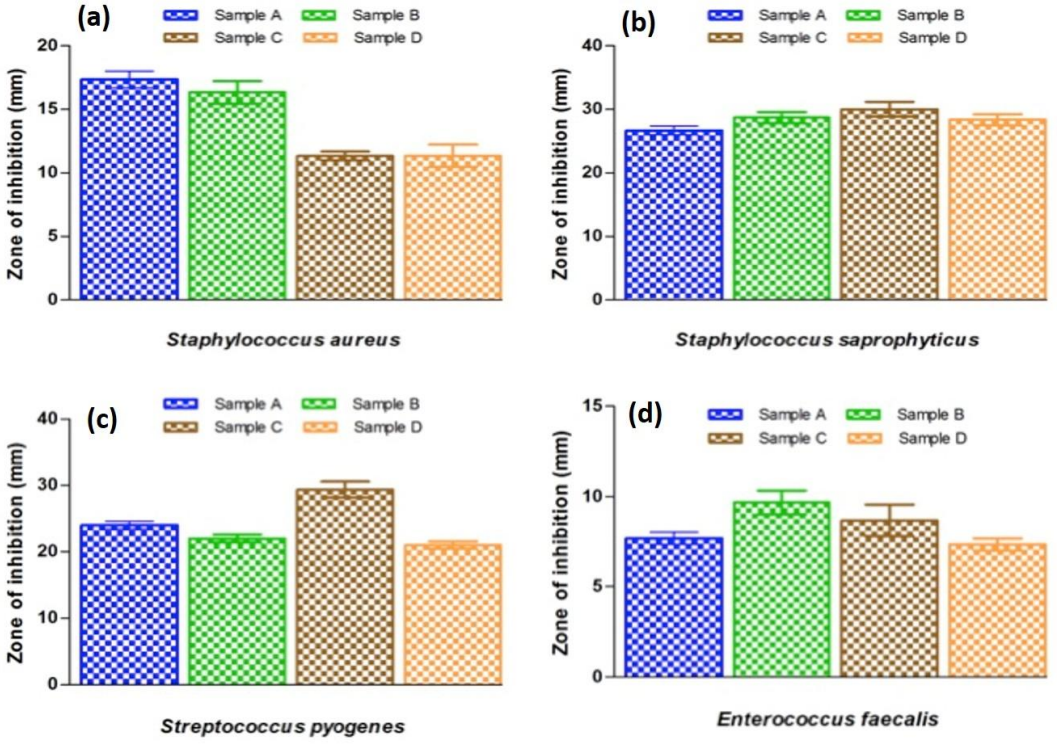


Fig. 7. Graphical summary of the inhibitory effect of synthesized compounds (A-D) on key Gram-positive bacterial pathogens, showing the variation in zone of inhibition diameters.

© Ariston Publications 2025. All rights reserved.

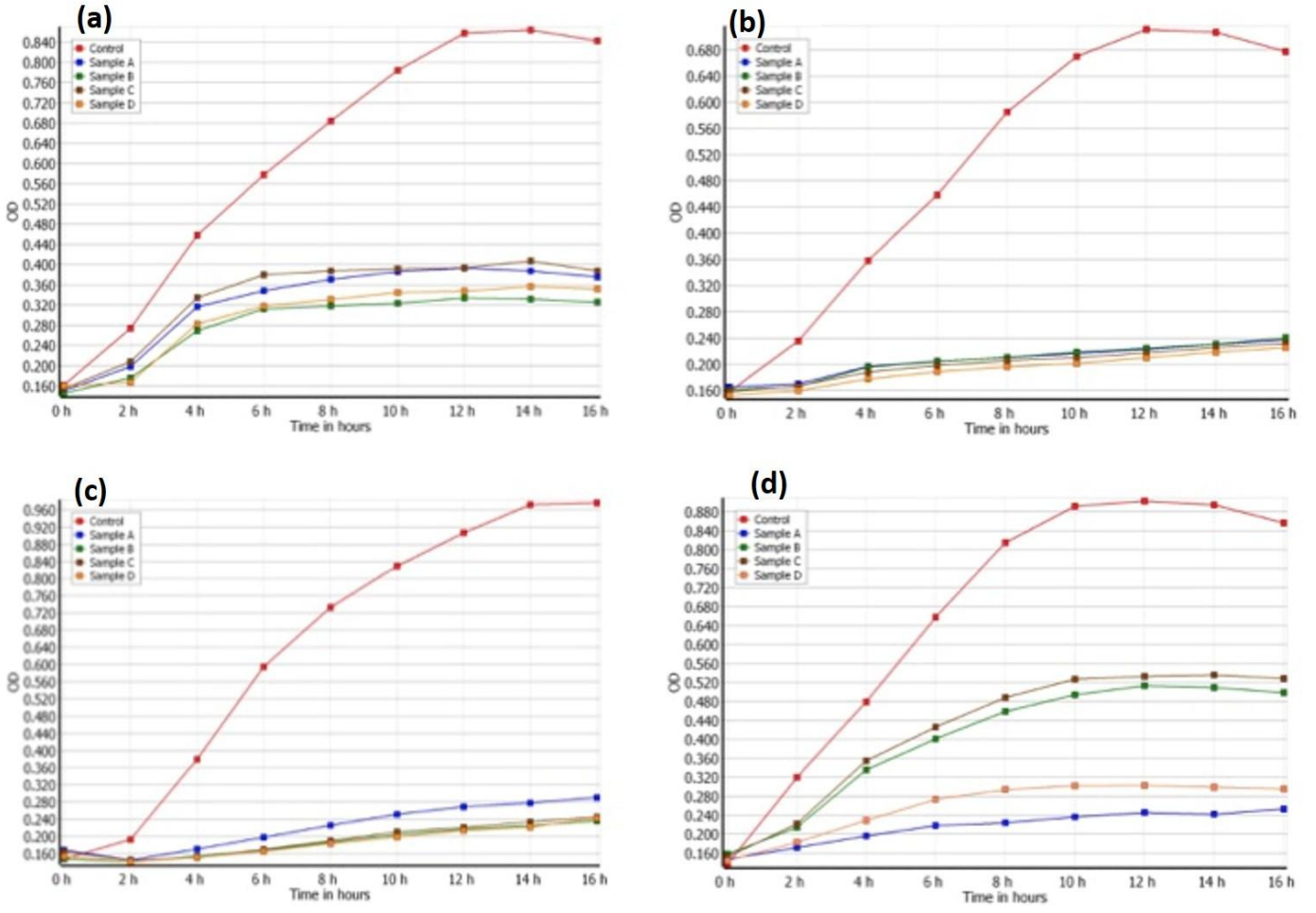


Fig. 8. Growth kinetics of Gram-positive bacteria treated with synthesized compounds. Graphs (A-D) show the optical density (OD600) over time for *Staphylococcus aureus*, *Staphylococcus saprophyticus*, *Streptococcus pyogenes*, and *Enterococcus faecalis*, respectively, when treated with Samples A-D compared to an untreated control.

The potency of the activity varied among the Gram-positive strains and between compounds. As summarized in Figure 7, the largest zones of inhibition, ranging from 26 to 30 mm in total diameter (corresponding to a 20-24 mm zone beyond the 6 mm well), were consistently observed against *S. saprophyticus*. *S. aureus* and *S. pyogenes* showed intermediate susceptibility, while *E. faecalis* was the least affected, with inhibition zones only 7 to 9 mm in total diameter. Among the compounds, Sample C (18PbO) tended to produce the largest zones, though the differences between samples were less pronounced than their differences in shielding performance [37-39]. This selective activity against Gram-positive bacteria is a common observation with many metallic ion-based antimicrobials and can be attributed to fundamental differences in cell wall structure [40, 41]. Gram-positive bacteria possess a thick, porous peptidoglycan layer that allows for easier penetration of antimicrobial ions like Ag^{+} or leached Pb^{2+}. Gram-negative bacteria, however, have an additional outer membrane composed of lipopolysaccharides (LPS) and phospholipids, creating a formidable permeability barrier that restricts the entry of many external agents, rendering them intrinsically more resistant.

3.3. Effect on Microbial Growth Kinetics

To complement the endpoint diffusion assay and understand the dynamic effect on bacterial proliferation, growth kinetic studies were performed. The growth curves for the susceptible Gram-positive bacteria (*S. aureus*, *S. saprophyticus*, *S. pyogenes*, and *E. faecalis*) in the presence of the glass compounds are presented in Figure 8. In these experiments, bacterial cultures at a standardized initial density were exposed to the compounds, and optical density (OD600) was monitored over 16 hours.

The results clearly demonstrate a bacteriostatic effect. For all four bacterial strains, the growth curves of cultures treated with any of the four glass compounds (Samples A-D) showed significant suppression compared to the untreated control. The lag phase was often prolonged, and the exponential growth phase was markedly attenuated, resulting in a substantially lower final cell density (lower plateau OD600) after 16 hours. This indicates that the compounds do not necessarily cause immediate cell death (bactericidal

© Ariston Publications 2025. All rights reserved.

action under these conditions) but severely inhibit cellular replication and metabolism [42]. The growth profiles for compounds within the same bacterial strain were similar, suggesting a common mechanism of action, likely the gradual release of biocidal metal ions (Ag^{+}, Pb^{2+}, Na^{+}) that interfere with vital cellular processes such as enzyme function, membrane integrity, and DNA replication. The fact that the inhibitory effects were most apparent during the logarithmic growth phase aligns with the general understanding that metabolically active, dividing cells are often more susceptible to antimicrobial agents [43].

3.4. Blood Coagulation Assay

The interaction of the glass components with the blood coagulation cascade was evaluated using two standard clinical tests: Prothrombin Time (PT) and Activated Partial Thromboplastin Time (APTT). PT assesses the extrinsic and common pathways, while APTT evaluates the intrinsic and common pathways. The results, presented in Figures 9 and 10, reveal a significant and compound-dependent modulation of clotting times.

For the PT assay (Figure 9), Samples A and B ($5Ag_2O$ and $7Na_2O$) showed clotting times of approximately 19 seconds each, which is within or near a typical normal reference range (often 11-13.5 seconds, but lab-dependent). This suggests they have little to no pro-coagulant effect on the extrinsic pathway. In striking contrast, Samples C and D (18PbO and 7PbO) dramatically shortened the PT to 8 and 12 seconds, respectively. A shortened PT indicates an acceleration of the extrinsic pathway, meaning these lead-containing compounds actively promote the initiation of coagulation via tissue factor (Factor VII) activation [44-48].

The APTT results (Figure 10) showed a different pattern. Samples A and B prolonged the APTT to 41 and 44 seconds, respectively, which is above the typical reference range (25-35 seconds). This suggests an inhibitory or anticoagulant effect on the intrinsic pathway (contact activation). Conversely, Samples C and D again demonstrated a strong pro-coagulant effect, significantly shortening the APTT to 27 and 29 seconds, well below the reference range. This indicates they also accelerate the intrinsic pathway.

The dual shortening of both PT and APTT by the lead-containing glasses (Samples C and D) is a strong indicator of a potent, broad-spectrum pro-coagulant activity. This could be due to several mechanisms. Lead ions (Pb^{2+}) may directly activate specific coagulation factors (such as Factor X or prothrombin), provide a surface that promotes the assembly of coagulation enzyme complexes (like the tenase and prothrombinase complexes), or initiate contact activation by providing a negatively charged surface. The anticoagulant effect seen with Samples A and B in the APTT assay is also noteworthy; silver ions (Ag^{+}) have been reported in some studies to exhibit antiplatelet properties, which could indirectly affect coagulation assays, though our test uses platelet-poor plasma [49, 50]. The sodium-based sample's effect may be related to ionic strength or other interfacial phenomena.

These findings have substantial implications. The potent pro-coagulant activity of the lead-doped glasses, particularly Sample C, suggests they could be engineered into topical hemostatic agents for controlling bleeding in surgical or trauma settings [44, 45]. However, the toxicity of lead is a severe limitation for any biomedical application. This highlights a critical trade-off: Sample C is the most effective radiation shield and the most potent pro-coagulant but is also the most toxic. This underscores the importance of future work to explore non-toxic heavy elements, such as Bismuth, Tungsten, that might mimic the shielding and potentially the pro-coagulant effects without the toxicity. The variable effects, anticoagulant for some, pro-coagulant for others, reinforce the concept that nanomaterial and ion interactions with the coagulation system are highly complex and composition-dependent, offering avenues for both hemostatic and antithrombotic applications [51-54].

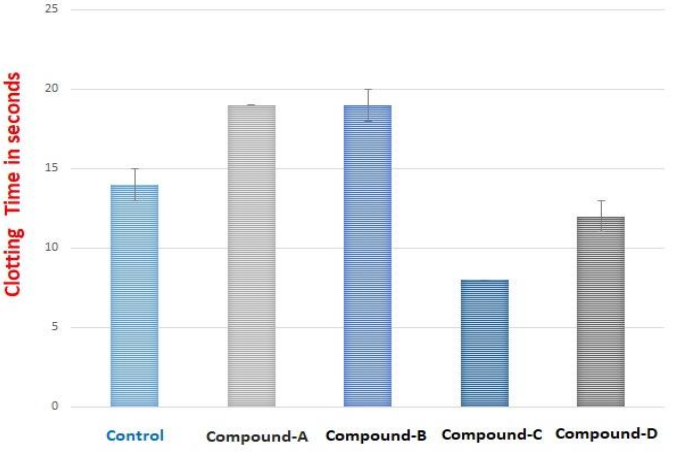


Fig. 9. Clotting times measured using the Prothrombin Time (PT) assay for compounds A-D, with normal plasma as a control. Error bars represent standard deviation.

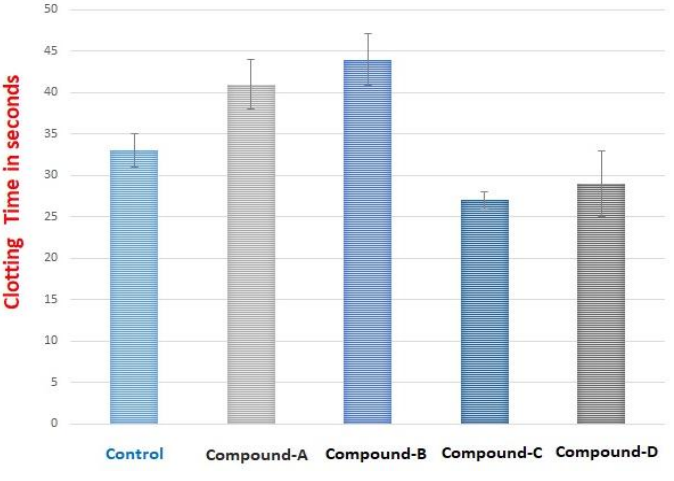


Fig. 10. Clotting times measured using the Activated Partial Thromboplastin Time (APTT) assay for compounds A-D, with normal plasma as a control. Error bars represent standard deviation.

© Ariston Publications 2025. All rights reserved.

This integrated study reveals the multifaceted nature of modified tellurite glasses. Sample C (18PbO) emerged as the superior material for gamma-ray shielding, exhibiting the highest MAC, LAC, Zeff, and Neff, along with the lowest HVL, TVL, and MFP. All glasses showed selective bacteriostatic activity against Gram-positive pathogens. Most significantly, the blood coagulation assays unveiled a stark functional divergence: the lead-containing glasses acted as potent pro-coagulants, while the silver and sodium variants showed neutral or mild anticoagulant effects. These results collectively position these materials, with careful consideration of their elemental toxicity, as promising candidates for further development in applications requiring combined radiation protection and bioactive functionality, such as in specialized medical environments or emergency response equipment.

4. CONCLUSION

This research systematically evaluated a series of tellurite glasses modified with Ag_2O, PbO, and Na_2O for their radiation shielding performance and in vitro biological properties. The photon attenuation characteristics, simulated across an energy range of 0.015 to 15 MeV, demonstrated that shielding efficiency is profoundly influenced by the composition and density of the glass. Specifically, the incorporation of a high lead oxide content (18 mol% PbO) yielded the most favorable outcomes, manifesting in the highest mass attenuation coefficients, the greatest effective atomic number, and the lowest half-value layer and mean free path among all tested samples. These findings underscore the critical role of heavy metal oxide modifiers in enhancing the gamma-ray interaction cross-section, making these glasses highly effective for shielding applications across a wide energy spectrum, from low-energy diagnostic ranges to high-energy therapeutic and industrial settings. Beyond their shielding utility, the biological assessment of these glasses revealed noteworthy in vitro activities. The compositions exhibited selective antibacterial effects, showing pronounced efficacy against several Gram-positive pathogens, which suggests potential for use in environments requiring antimicrobial surfaces. More significantly, the blood coagulation studies yielded compelling results. Specific glass formulations substantially reduced both prothrombin time (PT) and activated partial thromboplastin time (APTT), indicating a capacity to accelerate the intrinsic and extrinsic clotting pathways. This procoagulant activity highlights the potential of these materials to be engineered into hemostatic agents or coatings for medical devices to control bleeding. However, the dual nature of nanoparticle interactions with coagulation systems warrants careful consideration; while some compositions may aid hemostasis, others might require precise tuning to avoid undesirable thrombotic effects. In summary, this work presents a new class of multifunctional tellurite glasses that successfully merge significant radiation shielding capacity with beneficial biological activity. These results lay a strong foundation for the future development of advanced composite materials suitable for use in nuclear medicine, radiotherapy facilities, and as bioactive components in wound care or surgical applications, pending further in vivo validation and long-term biocompatibility studies.

DECLARATIONS

Ethical Approval

We affirm that this manuscript is an original work, has not been previously published, and is not currently under consideration for publication in any other journal or conference proceedings. All authors have reviewed and approved the manuscript, and the order of authorship has been mutually agreed upon.

Funding

Not applicable

Availability of data and material

The datasets used and/or analyzed during the current study are available from the corresponding author on reasonable request.

Conflicts of Interest

The authors declare that they have no financial or personal interests that could have influenced the research and findings presented in this paper. The authors alone are responsible for the content and writing of this article.

Authors' contributions

All authors contributed equally in the preparation of this manuscript.

ACKNOWLEDGEMENTS

The authors extend their appreciation to University Higher Education Fund for funding this research work under Research Support Program for Central labs at King Khalid University through the project number CL/PRI/B/3.

REFERENCES

[1] Rammah, Y.S., Sayyed, M.I., Abohaswa, A.S. and Tekin, H.O., 2018. FTIR, electronic polarizability and shielding parameters of B_2O_3 glasses doped with SnO_2. *Applied Physics A*, *124*(9), p.650.

© Ariston Publications 2025. All rights reserved.

[2] Zhang, A.Y. and Li, C.Y., 2014. Advances of study on the developments and physical properties of composite materials. *Applied Mechanics and Materials*, *633*, pp.379-382.

[3] Jayakumar, S., Saravanan, T. and Philip, J., 2023. A review on polymer nanocomposites as lead-free materials for diagnostic X-ray shielding: Recent advances, challenges and future perspectives. *Hybrid Advances*, *4*, p.100100.

[4] Sherer, M.A.S., Visconti, P.J., Ritenour, E.R. and Haynes, K.W., 2021. *Radiation Protection in Medical Radiography-E-Book: Radiation Protection in Medical Radiography-E-Book*. Elsevier Health Sciences.

[5] Santana, A., Alves-Pimenta, S., Martins, J., Colaço, B. and Ginja, M., 2021. Imaging diagnosis of canine hip dysplasia with and without human exposure to ionizing radiation. *The Veterinary Journal*, *276*, p.105745.

[6] Kawady, N.A., Elkattan, M., Salah, M. and Galhoum, A.A., 2022. Fabrication, characterization, and gamma ray shielding properties of PVA-based polymer nanocomposite. *Journal of Materials Science*, *57*(24), pp.11046-11061.

[7] McGregor, D. and Shultis, J.K., 2020. *Radiation detection: concepts, methods, and devices*. CRC Press.

[8] Harish, V., Nagaiah, N., Prabhu, T.N. and Varughese, K.T., 2009. Preparation and characterization of lead monoxide filled unsaturated polyester based polymer composites for gamma radiation shielding applications. *Journal of Applied Polymer Science*, *112*(3), pp.1503-1508.

[9] Yue, K., Luo, W., Dong, X., Wang, C., Wu, G., Jiang, M. and Zha, Y., 2009. A new lead-free radiation shielding material for radiotherapy. *Radiation protection dosimetry*, *133*(4), pp.256-260.

[10] Kim, Y., Park, S. and Seo, Y., 2015. Enhanced X-ray shielding ability of polymer–nonleaded metal composites by multilayer structuring. *Industrial & Engineering Chemistry Research*, *54*(22), pp.5968-5973.

[11] Uhm, Y.R., Kim, J., Lee, S., Jeon, J. and Rhee, C.K., 2011. In situ fabrication of surface modified lead monoxide nanopowder and its HDPE nanocomposite. *Industrial & Engineering Chemistry Research*, *50*(8), pp.4478-4483.

[12] Harish, V., Nagaiah, N., Prabhu, T.N. and Varughese, K.T., 2010. Thermo-mechanical analysis of lead monoxide filled unsaturated polyester based polymer composite radiation shields. *Journal of Applied Polymer Science*, *117*(6), pp.3623-3629.

[13] Yue, K., Luo, W., Dong, X., Wang, C., Wu, G., Jiang, M. and Zha, Y., 2009. A new lead-free radiation shielding material for radiotherapy. *Radiation protection dosimetry*, *133*(4), pp.256-260.

[14] El-Mallawany, R., Sayyed, M.I. and Dong, M.G., 2017. Comparative shielding properties of some tellurite glasses: Part 2. *Journal of Non-Crystalline Solids*, *474*, pp.16-23.

[15] Sayyed, M.I., Tekin, H.O. and Agar, O., 2019. Gamma photon and neutron attenuation properties of MgO–BaO–B_2O_3–TeO_2–Cr_2O_3 glasses: the role of TeO_2. *Radiation Physics and Chemistry*, *163*, pp.58-66.

[16] Gaikwad, D.K., Sayyed, M.I., Botewad, S.N., Obaid, S.S., Khattari, Z.Y., Gawai, U.P., Afaneh, F., Shirshat, M.D. and Pawar, P.P., 2019. Physical, structural, optical investigation and shielding featuresof tungsten bismuth tellurite based glasses. *Journal of Non-Crystalline Solids*, *503*, pp.158-168.

[17] Kurudirek, M., Chutithanapanon, N., Laopaiboon, R., Yenchai, C. and Bootjomchai, C., 2018. Effect of Bi_2O_3 on gamma ray shielding and structural properties of borosilicate glasses recycled from high pressure sodium lamp glass. *Journal of Alloys and Compounds*, *745*, pp.355-364.

[18] El-Mallawany, R., Sayyed, M.I. and Dong, M.G., 2017. Comparative shielding properties of some tellurite glasses: Part 2. *Journal of Non-Crystalline Solids*, *474*, pp.16-23.

[19] Tijani, S.A., Kamal, S.M., Al-Hadeethi, Y., Arib, M., Hussein, M.A., Wageh, S. and Dim, L.A., 2018. Radiation shielding properties of transparent erbium zinc tellurite glass system determined at medical diagnostic energies. *Journal of Alloys and Compounds*, *741*, pp.293-299.

[20] Zoulfakar, A.M., Abdel-Ghany, A.M., Abou-Elnasr, T.Z., Mostafa, A.G., Salem, S.M. and El-Bahnaswy, H.H., 2017. Effect of antimony-oxide on the shielding properties of some sodium-boro-silicate glasses. *Applied Radiation and Isotopes*, *127*, pp.269-274.

[21] Kumar, A., Kaur, R., Sayyed, M.I., Rashad, M., Singh, M. and Ali, A.M., 2019. Physical, structural, optical and gamma ray shielding behavior of (20+ x) PbO–10 BaO–10 Na_2O–10 MgO–(50-x) B_2O_3 glasses. *Physica B: Condensed Matter*, *552*, pp.110-118.

[22] Lakshminarayana, G., Baki, S.O., Lira, A., Kityk, I.V., Caldiño, U., Kaky, K.M. and Mahdi, M.A., 2017. Structural, thermal and optical investigations of Dy^{3+}-doped B_2O_3–WO_3–ZnO–Li_2O–Na_2O glasses for warm

 © Ariston Publications 2025. All rights reserved.

white light emitting applications. *Journal of Luminescence*, *186*, pp.283-300.

[23] Obaid, S.S., Sayyed, M.I., Gaikwad, D.K. and Pawar, P.P., 2018. Attenuation coefficients and exposure buildup factor of some rocks for gamma ray shielding applications. *Radiation Physics and Chemistry*, *148*, pp.86-94.

[24] Tekin, H.O., Kavaz, E., Altunsoy, E.E., Kilicoglu, O., Agar, O., Erguzel, T.T. and Sayyed, M.I., 2019. An extensive investigation on gamma-ray and neutron attenuation parameters of cobalt oxide and nickel oxide substituted bioactive glasses. *Ceramics International*, *45*(8), pp.9934-9949.

[25] Costa, F.B., Souza, A.K.R., Silva, J.R., Moraes, J.C.S., de Oliveira Nunes, L.A., da Cunha Andrade, L.H., El-Mallawany, R. and Lima, S.M., 2019. Effect of lithium addition on Te^{4+} emission in TeO_2-Li_2O glasses. *Journal of Non-Crystalline Solids*, *524*, p.119609.

[26] Dong, M., Elbashir, B.O. and Sayyed, M.I., 2017. Enhancement of gamma ray shielding properties by PbO partial replacement of WO3 in ternary $60TeO_2$–(40-x) WO_3–xPbO glass system. *Chalcogenide Lett*, *14*(3), pp.113-118.

[27] Rai, V.K., Rai, D.K. and Rai, S.B., 2006. Pr^{3+} doped lithium tellurite glass as a temperature sensor. *Sensors and Actuators A: Physical*, *128*(1), pp.14-17.

[28] Dong, M.G., Agar, O., Tekin, H.O., Kilicoglu, O., Kaky, K.M. and Sayyed, M.I., 2019. A comparative study on gamma photon shielding features of various germanate glass systems. *Composites Part B: Engineering*, *165*, pp.636-647.

[29] Agar, O., Khattari, Z.Y., Sayyed, M.I., Tekin, H.O., Al-Omari, S., Maghrabi, M., Zaid, M.H.M. and Kityk, I.V., 2019. Evaluation of the shielding parameters of alkaline earth based phosphate glasses using MCNPX code. *Results in Physics*, *12*, pp.101-106.

[30] Sayyed, M.I., Kumar, A., Tekin, H.O., Kaur, R., Singh, M., Agar, O. and Khandaker, M.U., 2020. Evaluation of gamma-ray and neutron shielding features of heavy metals doped Bi_2O_3-BaO-Na_2O-MgO-B_2O_3 glass systems. *Progress in Nuclear Energy*, *118*, p.103118.

[31] Kumar, A., Gaikwad, D.K., Obaid, S.S., Tekin, H.O., Agar, O. and Sayyed, M.I., 2020. Experimental studies and Monte Carlo simulations on gamma ray shielding competence of (30+ x) $PbO_{10}WO_3$ $10Na_2O-$ 10MgO–(40-x) B_2O_3 glasses. *Progress in Nuclear Energy*, *119*, p.103047.

[32] Prabhu, N.S., Hegde, V., Sayyed, M.I., Agar, O. and Kamath, S.D., 2019. Investigations on structural and radiation shielding properties of Er^{3+} doped zinc bismuth borate glasses. *Materials chemistry and physics*, *230*, pp.267-276.

[33] Tekin, H.O., Kavaz, E., Altunsoy, E.E., Kilicoglu, O., Agar, O., Erguzel, T.T. and Sayyed, M.I., 2019. An extensive investigation on gamma-ray and neutron attenuation parameters of cobalt oxide and nickel oxide substituted bioactive glasses. *Ceramics International*, *45*(8), pp.9934-9949.

[34] Kavaz, E., Tekin, H.O., Agar, O., Altunsoy, E.E., Kilicoglu, O., Kamislioglu, M., Abuzaid, M.M. and Sayyed, M.I., 2019. The Mass stopping power/projected range and nuclear shielding behaviors of barium bismuth borate glasses and influence of cerium oxide. *Ceramics International*, *45*(12), pp.15348-15357.

[35] Agar, O., Khattari, Z.Y., Sayyed, M.I., Tekin, H.O., Al-Omari, S., Maghrabi, M., Zaid, M.H.M. and Kityk, I.V., 2019. Evaluation of the shielding parameters of alkaline earth based phosphate glasses using MCNPX code. *Results in Physics*, *12*, pp.101-106.

[36] Al-Hadeethi, Y. and Sayyed, M.I., 2020. X-ray attenuation features of some tellurite glasses evaluated at medical diagnostic energies. *Applied Mathematics and Computation*, *365*, p.124712.

[37] Magaldi, S., Mata-Essayag, S., De Capriles, C.H., Pérez, C., Colella, M.T., Olaizola, C. and Ontiveros, Y., 2004. Well diffusion for antifungal susceptibility testing. *International Journal of Infectious Diseases*, *8*(1), pp.39-45.

[38] Ahmad, I., Wahab, S., Nisar, N., Dera, A.A., Alshahrani, M.Y., Abullias, S.S., Irfan, S., Alam, M.M. and Srivastava, S., 2020. Evaluation of antibacterial properties of Matricaria aurea on clinical isolates of periodontitis patients with special reference to red complex bacteria. *Saudi Pharmaceutical Journal*, *28*(10), pp.1203-1209.

[39] Zhang, H., Gruener, G. and Zhao, Y., 2013. Recent advancements of graphene in biomedicine. *Journal of Materials Chemistry B*, *1*(20), pp.2542-2567.

[40] Banerjee, M., Sharma, S., Chattopadhyay, A. and Ghosh, S.S., 2011. Enhanced antibacterial activity of bimetallic gold-silver core–shell nanoparticles at low silver concentration. *Nanoscale*, *3*(12), pp.5120-5125.

[41] Kumar, A., Vemula, P.K., Ajayan, P.M. and John, G., 2008. Silver-nanoparticle-embedded antimicrobial

© Ariston Publications 2025. All rights reserved.

paints based on vegetable oil. *Nature Materials*, *7*(3), pp.236-241.

[42] Das, M.R., Sarma, R.K., Saikia, R., Kale, V.S., Shelke, M.V. and Sengupta, P., 2011. Synthesis of silver nanoparticles in an aqueous suspension of graphene oxide sheets and its antimicrobial activity. *Colloids and Surfaces B: Biointerfaces*, *83*(1), pp.16-22.

[43] Roe, D., Karandikar, B., Bonn-Savage, N., Gibbins, B. and Roullet, J.B., 2008. Antimicrobial surface functionalization of plastic catheters by silver nanoparticles. *Journal of Antimicrobial Chemotherapy*, *61*(4), pp.869-876.

[44] Matter, M.T., Starsich, F., Galli, M., Hilber, M., Schlegel, A.A., Bertazzo, S., Pratsinis, S.E. and Herrmann, I.K., 2017. Developing a tissue glue by engineering the adhesive and hemostatic properties of metal oxide nanoparticles. *Nanoscale*, *9*(24), pp.8418-8426.

[45] Pourshahrestani, S., Zeimaran, E., Djordjevic, I., Kadri, N.A. and Towler, M.R., 2016. Inorganic hemostats: The state-of-the-art and recent advances. *Materials Science and Engineering: C*, *58*, pp.1255-1268.

[46] Pourshahrestani, S., Zeimaran, E., Kadri, N.A., Gargiulo, N., Samuel, S., Naveen, S.V., Kamarul, T. and Towler, M.R., 2016. Gallium-containing mesoporous bioactive glass with potent hemostatic activity and antibacterial efficacy. *Journal of Materials Chemistry B*, *4*(1), pp.71-86.

[47] Howe, N. and Cherpelis, B., 2013. Obtaining rapid and effective hemostasis: Part I. Update and review of topical hemostatic agents. *Journal of the American Academy of Dermatology*, *69*(5), pp.659-e1.

[48] Hoffman, M., 2003. Remodeling the blood coagulation cascade. *Journal of thrombosis and thrombolysis*, *16*(1), pp.17-20.

[49] Ragaseema, V.M., Unnikrishnan, S., Krishnan, V.K. and Krishnan, L.K., 2012. The antithrombotic and antimicrobial properties of PEG-protected silver nanoparticle coated surfaces. *Biomaterials*, *33*(11), pp.3083-3092.

[50] Shrivastava, S., Bera, T., Singh, S.K., Singh, G., Ramachandrarao, P. and Dash, D., 2009. Characterization of antiplatelet properties of silver nanoparticles. *ACS Nano*, *3*(6), pp.1357-1364.

[51] Asaduzzaman, M., Bappy, S.R., Fatema, B., Haque, S., Islam, M.J., Sikder, M.A., Aktar, S., Khatun, M., Juliana, F.M. and Islam, M.S., 2017. Effect of hepatitis C virus (HCV) on hemoglobin, blood cells and random blood glucose levels among serologically positive HCV patients. *IOSR Journal of Nursing and Health Science (IOSR-JNHS)*, *6*(5), pp.41-45.

[52] Fischbach, F.T. and Dunning, M.B., 2009. *A manual of laboratory and diagnostic tests*. Lippincott Williams & Wilkins.

[53] Pagana, K.D., Pagana, T.J. and Pagana, T.N., 2019. Mosby's Diagnostic & Laboratory Test Reference. 14th edn St. *Louis, Mo: Elsevier*.

[54] K Kamal, A.H., Tefferi, A. and Pruthi, R.K., 2007, July. How to interpret and pursue an abnormal prothrombin time, activated partial thromboplastin time, and bleeding time in adults. In *Mayo Clinic Proceedings* (Vol. 82, No. 7, pp. 864-873). Elsevier.

 © Ariston Publications 2025. All rights reserved.